

Kelvin–Helmholtz waves in extratropical cyclones passing over mountain ranges

Socorro Medina^a and Robert A. Houze, Jr.^{a,b*}

^aDepartment of Atmospheric Sciences, University of Washington, Seattle, WA, USA

^bPacific Northwest National Laboratory, Richland, WA, USA

*Correspondence to: R. A. Houze, Jr., 604 ATG Bldg., Box 351640, 3920 Okanogan Lane NE, Seattle, Washington 98195-1640 USA.
E-mail: houze@uw.edu

Kelvin–Helmholtz billows with horizontal scales of 3–4 km have been observed in midlatitude cyclones moving over the Italian Alps and the Oregon Cascades when the atmosphere was mostly statically stable with high amounts of shear and $Ri < 0.25$. In one case, data from a mobile radar located within a windward facing valley documented a layer in which the shear between down-valley flow below 1.2 km and strong upslope cross-barrier flow above was large. Several episodes of Kelvin–Helmholtz waves were observed within the shear layer. The occurrence of the waves appears to be related to the strength of the shear: when the shear attained large values, an episode of billows occurred, followed by a sharp decrease in the shear. The occurrence of large values of shear and Kelvin–Helmholtz billows over two different mountain ranges suggests that they may be important features occurring when extratropical cyclones with statically stable flow pass over mountain ranges.

Key Words: orographic precipitation; Kelvin–Helmholtz; extratropical cyclone

Received 10 September 2015; Revised 8 December 2015; Accepted 4 January 2016; Published online in Wiley Online Library 19 February 2016

1. Introduction

Kelvin–Helmholtz (KH) instability manifests as billow structures in a variety of atmospheric phenomena, and they are sometimes recognizable in radar displays. According to Browning and Watkins (1970):

Kelvin–Helmholtz instability is a form of dynamic instability produced within a hydrostatically stable flow in the presence of sufficiently large values of vertical shear. It appears as amplifying waves ('billows') oriented perpendicular to the shear vector, into which the vorticity is concentrated, and which eventually 'break' into turbulent flow on a range of smaller scales.

Seminal studies in the early 1970s documented the occurrence of Clear Air Turbulence (CAT), a manifestation of KH instability (e.g. Atlas *et al.*, 1970; Browning and Watkins, 1970; Dutton and Panofsky, 1970; Browning, 1971). KH waves have now been observed within the clouds of fronts, cumulonimbus anvils, hurricanes, sea breezes and winter storms, among others (e.g. Sha *et al.*, 1991; Chapman and Browning, 1997, 1999; Petre and Verlinde, 2004; Aberson and Halverson, 2006; Geerts and Miao, 2010; Houser and Bluestein, 2011; Zagrodnik *et al.*, 2015). Some of the most extensive and higher-resolution observations of KH waves have been collected with the United Kingdom (UK) Chilbolton Doppler radar, which has a very narrow beam width (0.28°) and hence extremely high spatial resolution. For example, Figure 1 from Chapman and Browning (1997) shows the radial velocity and the vertical shear structure associated with KH waves

in a warm frontal cloud system as captured by the Chilbolton radar. The objective of this study is to present radar evidence that KH waves of the type seen by Chapman and Browning (1997) occur in winter cyclonic storms passing over mountain ranges and to investigate how the vertical shear intensification over the windward slopes of mountain ranges relates to the KH waves.

2. Data and methodology

The data used in this study were collected in two field projects. One was the Mesoscale Alpine Programme (MAP; Bougeault *et al.*, 2001) conducted over the southern European Alps (Figure 2(a) and (b)) in the autumn of 1999. The other was the second phase of the Improvement of Microphysical Parameterization through Observational Verification Experiment (IMPROVE-2; Stoelinga *et al.*, 2003) conducted over the Oregon Cascades (Figure 2(c)) in the winter of 2001. Both projects sought to gain a better understanding of the dynamical and microphysical processes that occur when a baroclinic midlatitude cyclone encounters a major mountain range. Figure 2(b) and (c) show the location of the main instruments used in this study: upstream soundings (SND) and the National Center for Atmospheric Research (NCAR) S-band dual-polarization Doppler radar (S-Pol, with wavelength = 10 cm and beam width = 0.9°). The S-Pol scanning strategy during MAP consisted of several predefined Plan Position Indicator (PPI) scans and of Range–Height Indicator (RHI) scans whose locations were manually adjusted to cover the region of heaviest orographic precipitation. During IMPROVE-2, the S-Pol scanning strategy normally consisted of three low-level PPI scans, an

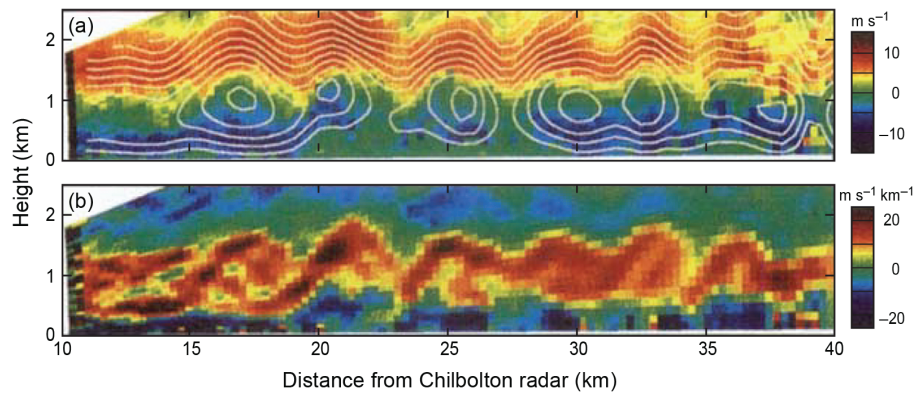


Figure 1. Vertical RHI scan collected by Chilbolton radar at 2220 UTC 6 September 1995 for an azimuth of 90.0° . (a) Radial velocity, where negative velocities are toward the radar (i.e. from right to left) and positive velocities are away from the radar. The contours are of mass-stream-function projected onto the plane of the RHI. (b) Vertical wind shear. From Chapman and Browning (1997).

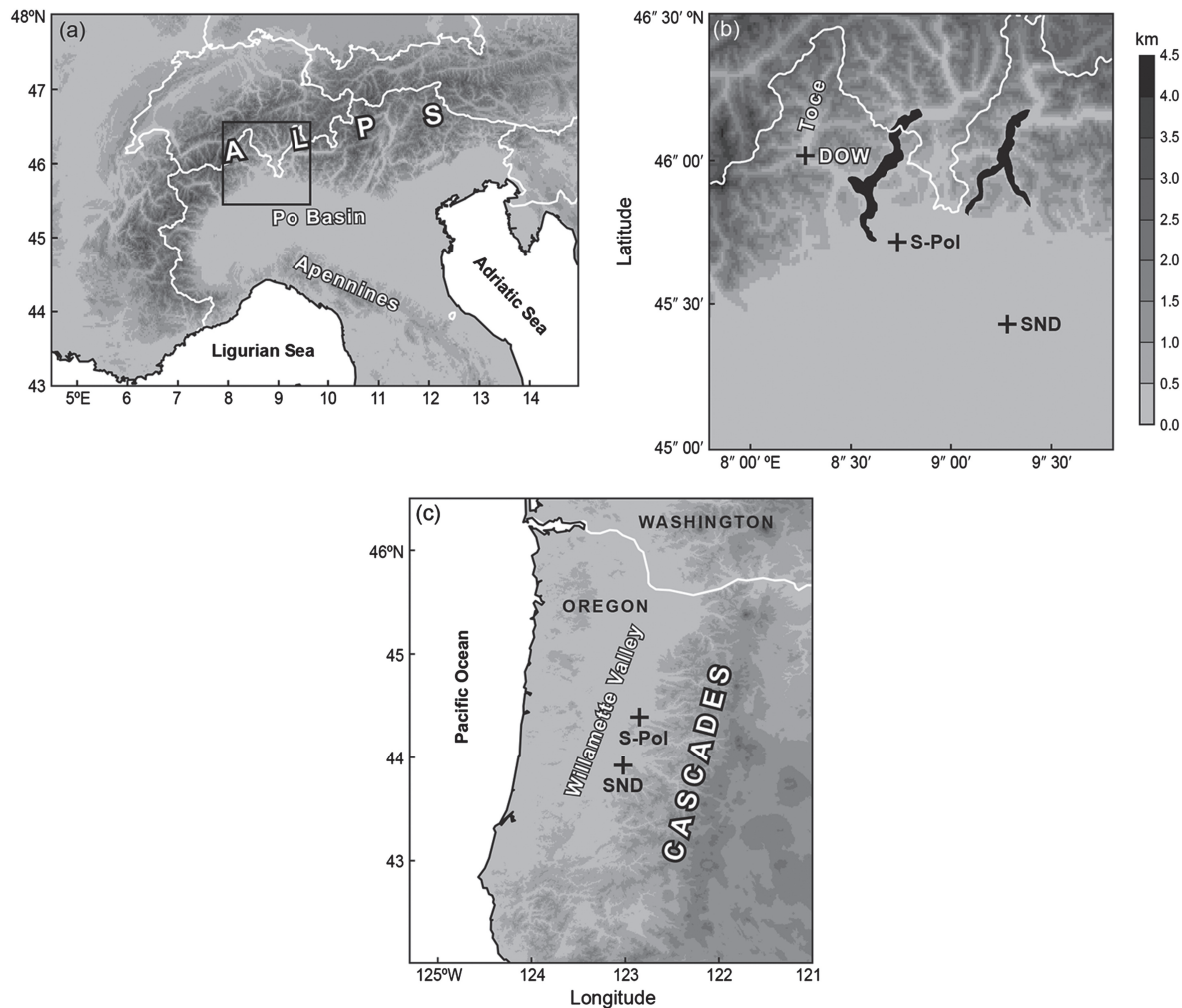


Figure 2. Topography and relevant geographic features of the areas where KH waves were observed. (a) European Alps, where the inset indicates the location of the area displayed in (b). (c) Oregon Cascades. The location of the S-Pol radar (S-Pol) and the upper-air sounding (SND) are indicated in (b) and (c).

eastward-looking sector consisting of 60 RHI scans at 1° azimuth intervals and one westward-looking RHI scan. During the MAP case described in this article, the X-band Doppler-on-Wheels (DOW, with wavelength = 3 cm and beam width = 0.9°) radar (Wurman *et al.*, 1997) was deployed inside the Toce Valley (Figure 2(b)). Its scanning strategy consisted of one multi-elevation volume PPI scan interspersed with RHI scans pointing up, down and across the valley (Steiner *et al.*, 2003).

3. Radar observation of Kelvin–Helmholtz waves

In this article we analyse two case-studies of orographic storms that have been previously studied in the literature:

- Alpine case – MAP Intensive Observing Period (IOP) 8, which occurred on 20/21 October 1999. This case occurred as a midlatitude cyclone approached the Alps (Figure 3(a) and (c)) and is one of the first and best documented cases exhibiting down-valley flow in the presence of synoptic flow toward a mountain range during the passage of a frontal system (e.g. Bousquet and Smull, 2003a, 2003b, 2006; Steiner *et al.*, 2003; Asencio and Stein, 2006).
- Cascade case – This event occurred as a midlatitude cyclone approached the Oregon Cascades on 28/29 November 2001 (Figure 3(b) and (d)), and it produced some of the largest precipitation accumulations observed during IMPROVE-2 (Houze and Medina, 2005). Although

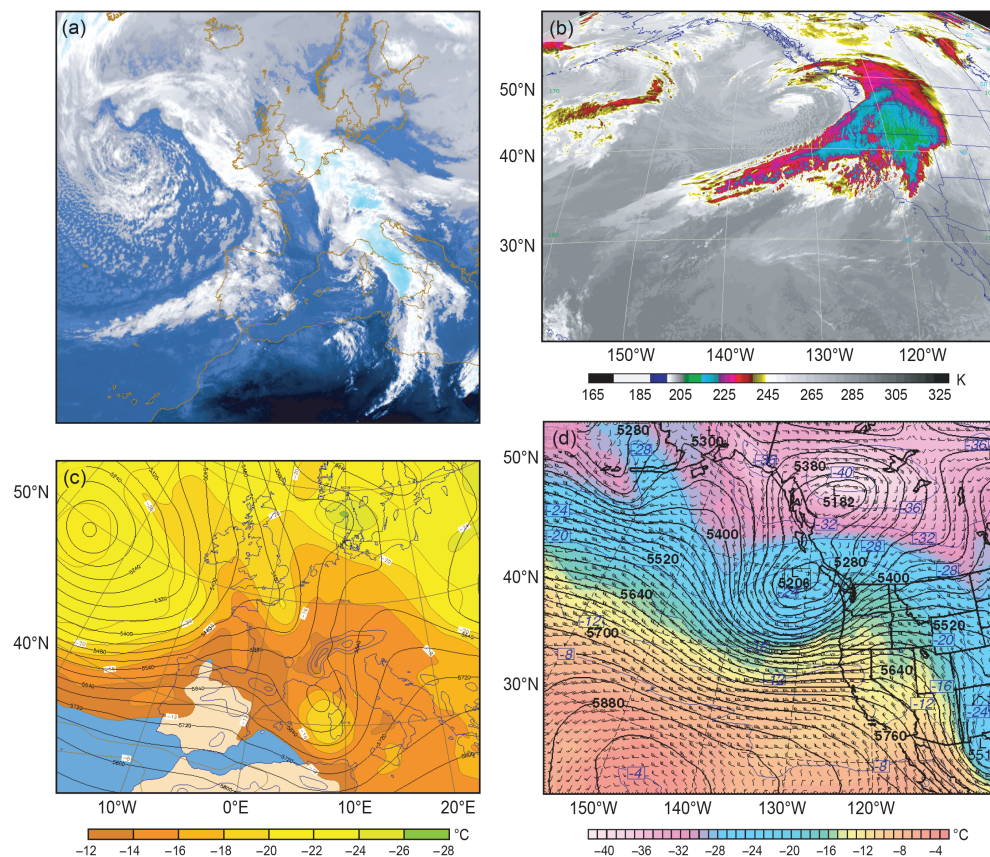


Figure 3. Synoptic set-up of the (a,c) Alpine and (b,d) Cascade case-studies. Infrared satellite images at (a) 1200 UTC 21 October 1999 and (b) 1700 UTC 28 November 2001. 500 hPa geopotential height (black contours) and air temperature degrees Celsius (colour shading) from (c) European Centre for Medium-Range Weather Forecasts valid at 1200 UTC 21 October 1999 and (d) University of Washington operational forecast valid at 1800 UTC 28 November 2001.

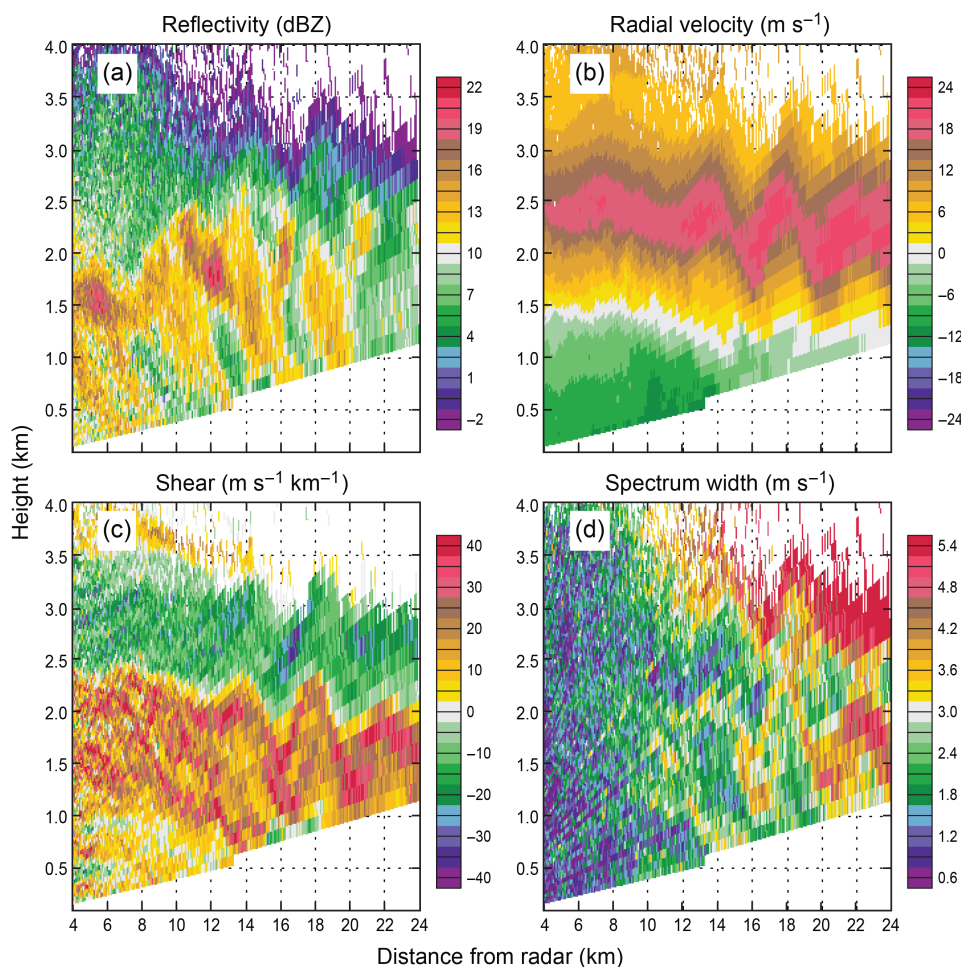


Figure 4. Alpine case RHI scan collected with the DOW radar in the down-valley direction showing (a) reflectivity, (b) radial velocity, (c) radial velocity shear and (d) spectrum width at 0728 UTC 21 October 1999. Negative radial velocities are toward the radar (i.e. from right to left) and positive velocities are away from the radar. See text for details on radial velocity shear calculation.

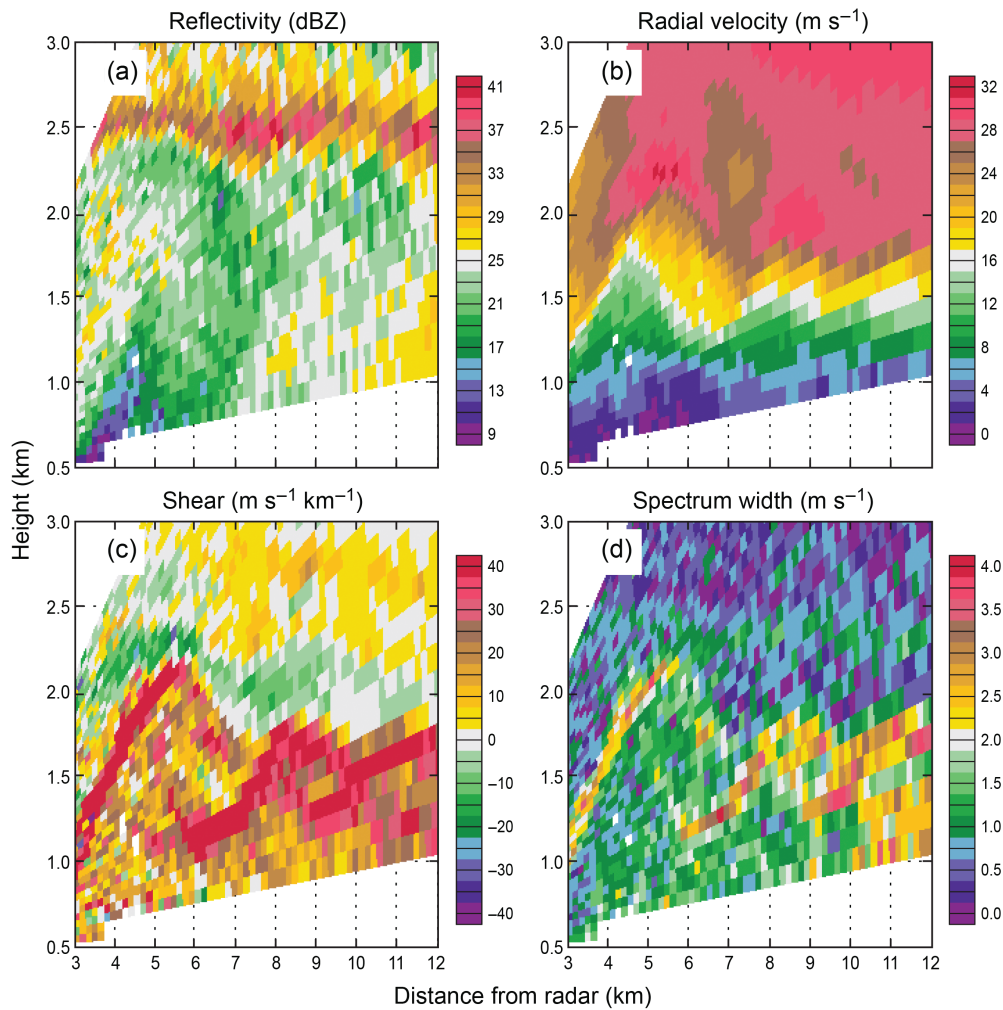


Figure 5. As in Figure 4 but for the Cascade case. The data was collected with the S-Pol radar in a scan looking due eastward at 1500 UTC 28 November 2001.

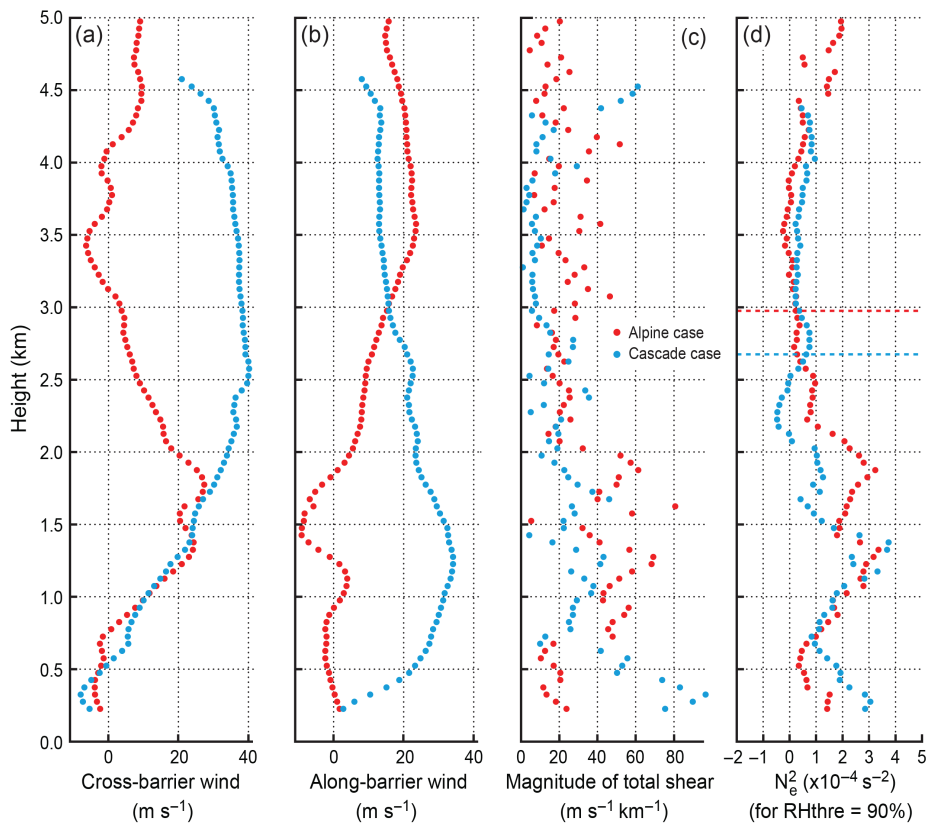


Figure 6. (a–d) Upstream soundings launched from the SND locations in Figure 2 collected during the Alpine (0600 UTC 21 October 1999) and Cascade (1726 UTC 28 November 2001) cases. The sounding data were interpolated to a regular vertical grid to facilitate calculations. In addition, the temperature data were filtered with a running mean to facilitate the calculation of derivatives. RHthre is the threshold relative humidity used in calculating the effective static stability.

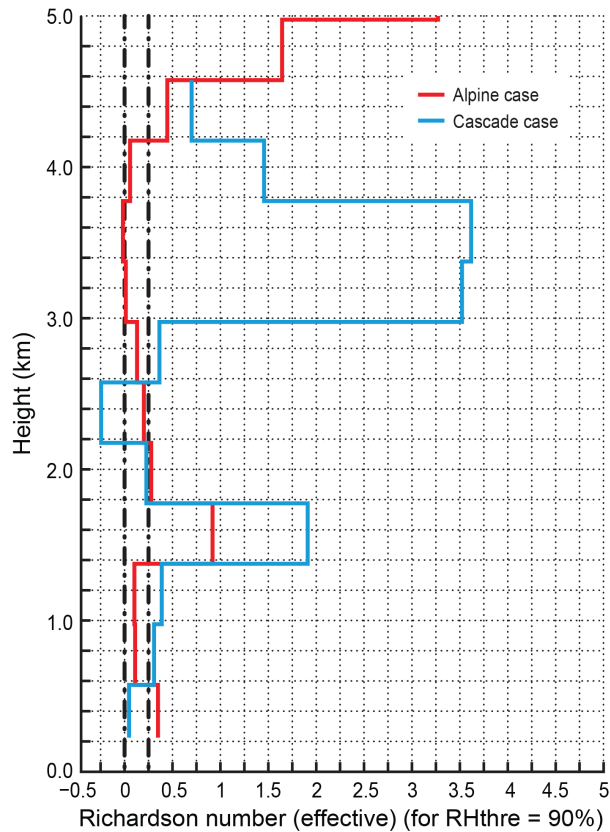


Figure 7. Vertical profiles of Richardson number for the soundings shown in Figure 6 calculated for layers 0.4 km deep. RH_{thre} is the threshold relative humidity used in calculating the effective static stability.

Table 1. Critical levels characteristics.

	Layer name	Critical level (km)	Thickness (<i>h</i>) (km)	Wavelength range of most unstable wave (6.3–7.5 <i>h</i>) (km)
Alpine case	Layer A	0.6–1.4	0.8	5.0–6.0
	Layer B	2.2–3.4	1.2	7.6–9.0
	Layer C	3.8–4.2	0.4	2.6–3.0
Cascade case	Layer A	0.2–0.6	0.4	2.5–3.0
	Layer B	1.8–2.2	0.4	2.5–3.0

there is no documentation of down-valley flow during this case, there is evidence that the low-level flow was strongly retarded near the terrain (e.g. Fig. 7e of Houze and Medina, 2005), with a large-shear layer between the retarded low-level flow and the stronger cross-barrier flow at slightly higher levels. Further details of this case are described by Medina *et al.* (2005, 2007).

Although these case-studies were collected a few years ago, the detailed and *in situ* data that were collected have not yet been fully analysed and there is rich information that still remains to be extracted from these datasets. As has been documented in the literature cited above, both of these case-studies featured widespread precipitation, often with a well-defined bright band, characteristic of stratiform precipitation. In addition, the precipitation field was punctuated by embedded convection. Figure 4 shows a vertical cross-section of DOW radar data looking straight down the Toce Valley (Figure 2(b)) during the Alpine Case. The reflectivity (Figure 4(a)) does not display a bright band at the time shown; however, there is clear evidence of it at other times (e.g. Fig. 20b of Houze and Medina, 2005). The radial velocity indicated flow away from the radar below 1.5 km (that is, down-valley flow) and there was an undulating jet toward the radar above this level, centred around 2.5 km (Figure 4(b)). From this figure it is evident that the vertical shear in the layer between 1 and 2.5 km was large. The radial velocity shear was calculated

as the difference in the radial velocities between gates adjacent in elevation divided by the vertical distance separating the gates. Figure 4(c) shows shear values reaching $40 \text{ m s}^{-1} \text{ km}^{-1}$ and a ‘braided’ or shear-splitting structure similar to what Chapman and Browning (1997, 1999) saw in association with KH waves. The typical wavelength of the observed waves was $\sim 4 \text{ km}$. A braided structure is also suggested in the spectrum width (Figure 4(d)).

For the Cascade case, we present a cross-section of S-Pol radar data that extends from the radar due eastward, toward the Cascades (Figure 2(c)). A reflectivity bright band was clearly observed at a height of 2.5 km (Figure 5(a)). The low-level flow, which was retarded by terrain, was nearly zero, while the flow above had a strong westerly component (Figure 5(b)). Between these two flows there was a layer with large values of shear. Large shear values and shear-splitting structures were clearly seen in the radial velocity shear with typical wavelengths of $\sim 3 \text{ km}$ (Figure 5(c)). A braided structure was also seen in the spectrum width (Figure 5(d)).

4. Sounding observations

The upstream conditions of the flow were recorded by special soundings launched from the locations labelled with SND in Figure 2(b) and (c) in the Alpine and Cascade cases, respectively. For the Alpine case, the orientation of the barrier used to calculate the cross- and along-barrier wind components was southwest–northeast, as noted in Medina and Houze (2003). In the Cascades case, the barrier has a north–south orientation. The cross-barrier flow components were slightly negative near the surface and increased rapidly with height in both cases (Figure 6(a))[†], further illustrating the shear layers that were seen in Figures 4(b) and 5(b). For the Alpine case there was a cross-barrier jet at $\sim 1.8 \text{ km}$ above the Po Basin, which was a lower altitude than that of the jet seen inside the Toce Valley (Figure 4(b)), suggesting that the cross-barrier jet was climbing over the terrain. For the Cascade case, there is evidence of a barrier-parallel jet around 1.2 km (Figure 6(b)), similar to what was seen in other IMPROVE-2 cases (e.g. Garvert *et al.*, 2005a, 2005b, 2007) and in some California Sierra Nevada events (e.g. Kingsmill *et al.*, 2013; Neiman *et al.*, 2013; Medina and Houze, 2015). According to the sounding data, the magnitude of the total vertical shear reached values as high as 40 and even $80 \text{ m s}^{-1} \text{ km}^{-1}$ at some levels (Figure 6(c)).[‡] While the magnitude of the total vertical shear is by definition always positive, the calculation of the radial velocity shear can be positive or negative. However, the magnitude of the total vertical shear measured with the sounding (Figure 6(c)) and the radial velocity shear (Figures 4(c) and 5(c)) are in agreement in the fact that there are large shears in the 1–2 km layers. Figure 6(d) shows the effective stability N_e^2 , which is the square of the dry Brunt–Väisälä frequency if the relative humidity is less than 90% and is the moist version otherwise (as in Medina and Houze, 2015). The stability profiles for both cases are very similar. For the Alpine case, there was very slight instability in the layer ~ 3.2 –3.8 km. For the Cascade case there was a small amount of instability $\sim 0.4 \text{ km}$ below the 0°C level (which was at $\sim 2.7 \text{ km}$), probably related to overturning associated with melting and diabatic cooling, similar to that found by Medina and Houze (2015). Other than in those layers, the conditions were for the most part statically stable and the stability was particularly strong between ~ 1 and 2 km (N_e^2 reaching $> 2 \times 10^{-4} \text{ s}^{-2}$ averaged over that layer), i.e. near the levels where the KH waves were observed in Figures 4(c) and 5(c).

The Richardson number, $Ri \equiv N_e^2 / (du/dz)^2$, considers the combined effects of the stability and the magnitude of the

[†]The soundings presented in Figure 6 are the ones closest in time to the time stamps of Figures 4 and 5; however, the Alpine sounding was obtained $\sim 1.5 \text{ h}$ before the time depicted in Figure 4, while the Cascade sounding was taken 2.5 h after the time shown in Figure 5.

[‡]The magnitude of the total vertical shear is by definition always positive. This convention is different from the ‘radial velocity shear’ shown in Figures 1(b), 4(c) and 5(c), which can be positive or negative.

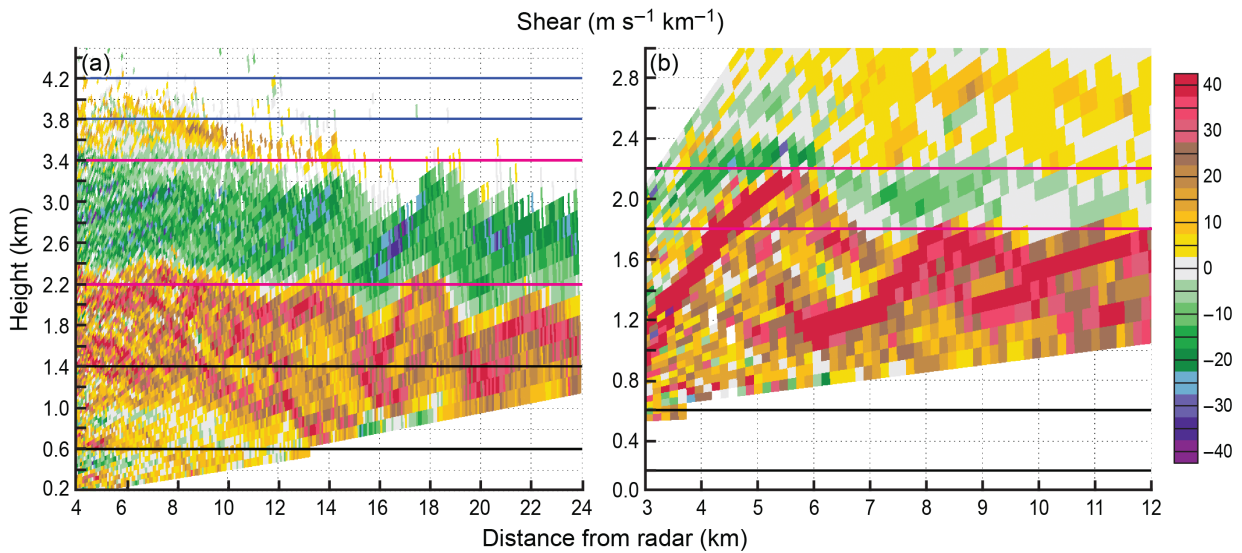


Figure 8. Radial velocity shear for (a) the Alpine case (as shown in Figure 4(c)), and (b) the Cascade case (as shown in Figure 5(c)). The horizontal lines mark the top and bottom of the critical levels given in Table 1. Layer A is indicated with black lines, layer B with pink lines, and layer C with blue lines.

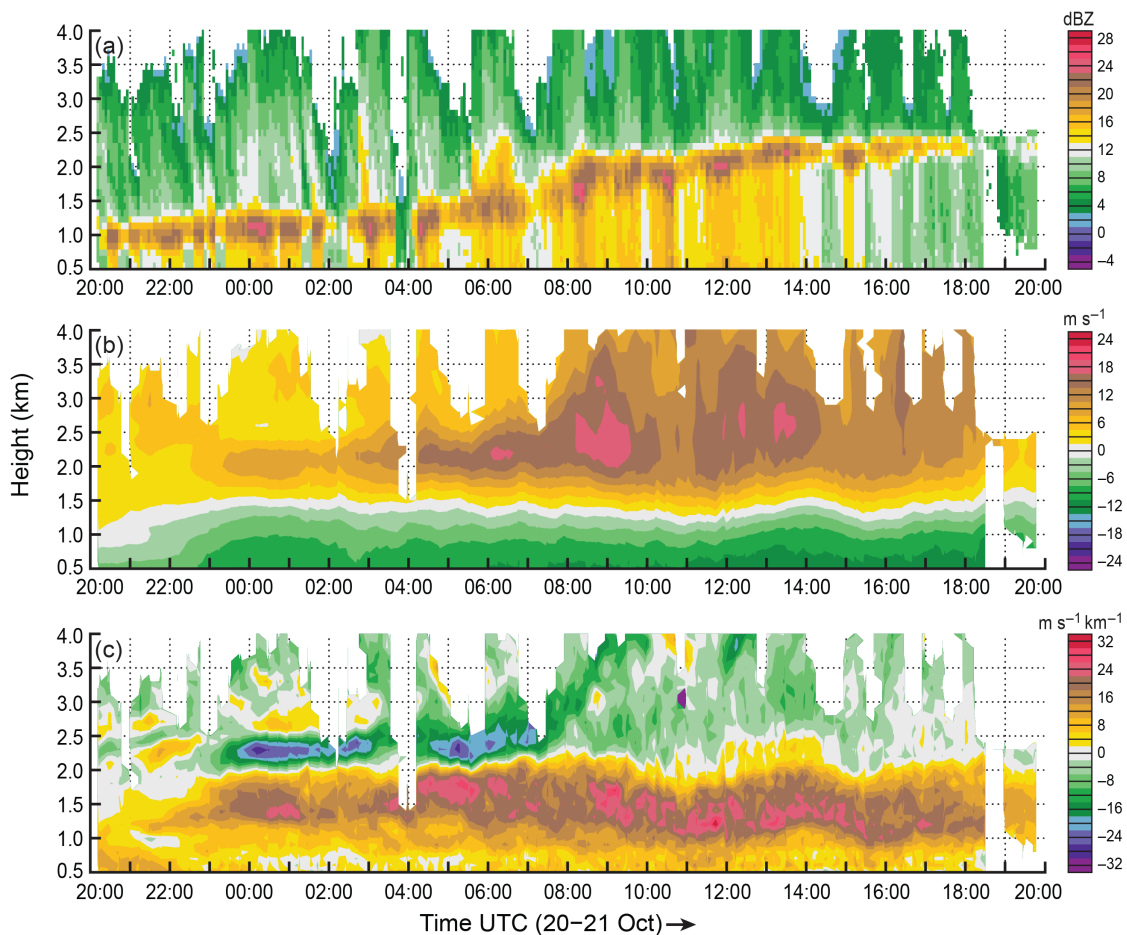


Figure 9. Time–height plot of down-valley DOW averaged (a) reflectivity and (b) radial velocity. The details on how the average was constructed are discussed in the text. (c) Shear calculated from the averaged radial velocity data shown in (b).

total vertical shear. KH instability may develop when $Ri < 0.25$ (Miles and Howard, 1964). According to Turner (1973) the horizontal wavelength λ of the most unstable wave is in the range: $6.3h < \lambda < 7.5h$, where h is the thickness of the layer where $Ri < 0.25$. The KH waves observed in Figures 4 and 5 had wavelengths $\lambda \sim 3\text{--}4$ km, hence the expected h is in the range $\sim 0.4\text{--}0.6$ km. Following Browning (1971), we examine sounding information over vertical layers with a depth comparable to the vertical dimension of the dynamically unstable layers. The data shown in Figure 6 were then used to calculate Ri over vertical layers with a depth of 0.4 km (Figure 7). The critical levels, i.e. the layers

in which $Ri < 0.25$, and the expected wavelength range of the most unstable waves, are listed in Table 1. These layers are indicated in Figure 8 along with the radial velocity shear (reproduced from Figures 4(c) and 5(c)). It may be argued that for both cases, the lower layer (indicated in horizontal black lines and called Layer A in Table 1) is the one that is responsible for the KH billows seen in Figure 8. Although the critical levels labelled as ‘A’ occurred at lower levels than where the KH billows occurred, the offset is not surprising given that the soundings represent the flow upstream of the terrain (Figure 2(b) and (c)). It is expected that the flow would be subject to orographic lifting farther downstream. For

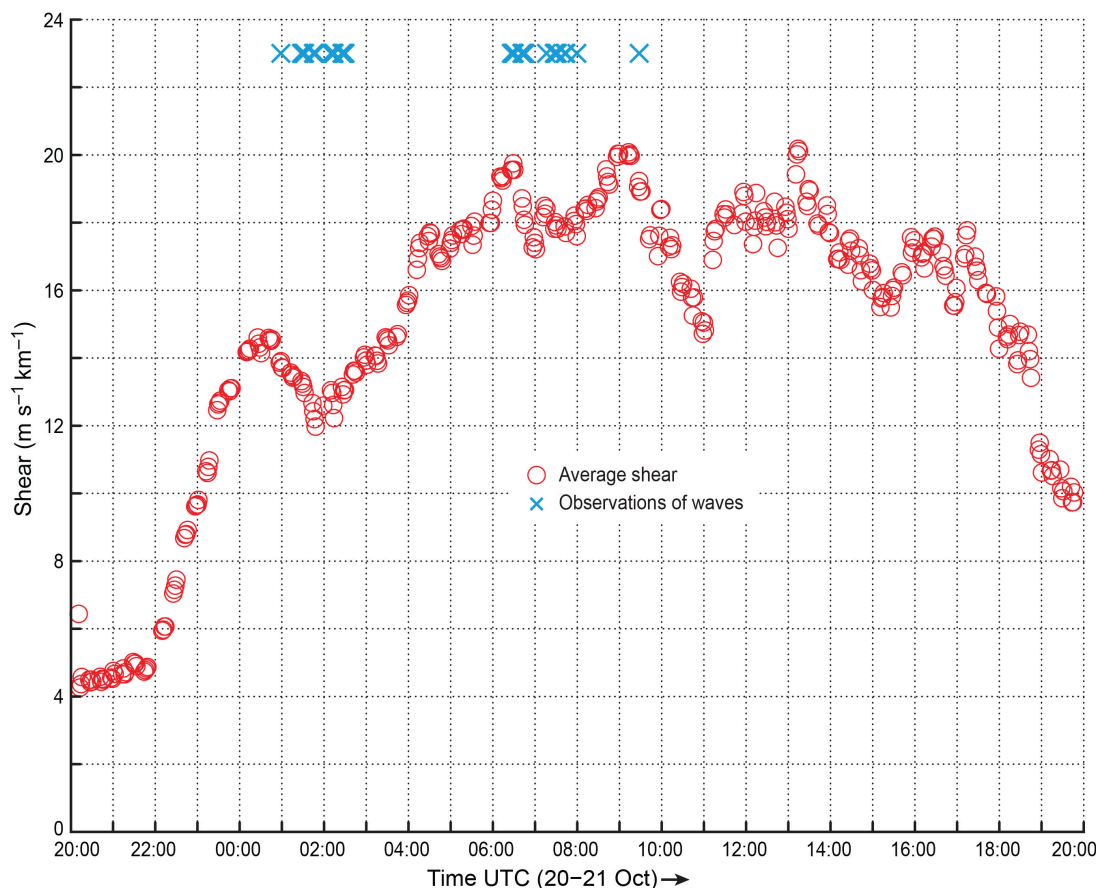


Figure 10. Evolution of the mean radial velocity shear for the Alpine case-study shown by red circles (calculated from averaging the data in Figure 9(c) in the vertical layer between 0.8 and 2.0 km). Each blue x shows a clearly identified occurrence of KH billows in the DOW radar radial velocity data.

the current cases, it is expected that the orographic lifting of the billows could be $\sim 0.5\text{--}1$ km, which is roughly consistent with the offset seen in Figure 8 between the KH billow and the critical levels labelled A. A more exact calculation is difficult given that it depends greatly on the local troughs and valleys of the terrain. Indeed, Geerts and Miao (2010) found a similar displacement that was attributed to orographic lifting of the upstream flow. As indicated in Table 1, the wavelength range associated with Layer A is 5.0–6.0 km for the Alpine case (2.5–3.0 km for the Cascade case), i.e. relatively consistent with the observed wavelength of 4 km (3 km). The thickness of these layers is 0.8 and 0.4 km for the Alpine and Cascade cases, respectively, which matches to some degree the expected h range of $\sim 0.4\text{--}0.6$ km. In looking at these expected ranges and wavelengths, it is important to consider that although the criterion of $Ri < 0.25$ is commonly used to assess when KH instability will occur, it should not be taken too strictly, since the exact criterion is difficult to establish in nonlinear three-dimensional flow (e.g. Miles, 1986), with additional complications in moist flows. In addition, the computation of bulk Ri is very sensitive to the vertical resolution used (e.g. Reiter and Lester, 1968; Gage and Van Zandt, 1983; Werne and Fritts, 1999).

5. Co-evolution of shear and KH waves

During the Alpine case, the DOW radar mapped the down-valley flow with relatively high temporal resolution, allowing us to study the co-evolution of the shear and the KH waves within the Toce Valley. A DOW RHI scan was typically obtained every 1.5 min[§]. In addition, the relatively simple geometry of the Toce valley constrained the flow to two dimensions, which facilitates studying the relationship between the magnitude of the shear

and the occurrence of the KH billows. For each down-valley RHI scan (as in Figure 4(b)), we constructed a mean vertical profile of reflectivity and radial velocity by averaging all the observations whose x -axes were between 5 and 20 km from the radar.[¶] These ranges were selected to avoid including the data collected (i) very near the radar because it had some noise and (ii) farthest from the radar because it did not provide information at the highest levels. The vertical grid used to calculate the averages was 0.01 km. Figure 9(a) shows that throughout most of the period shown there was a well-defined bright band whose height increased with time as a pre-existing cold low-level mass of air that was trapped inside the Po Basin was eroded when the baroclinic storm moved over the area (Bousquet and Smull, 2006). The averaged radial velocity shows there was persistent down-valley flow below ~ 1.2 km (Figure 9(b)). Above 1.2 km there was up-valley flow (Figure 9(b)). Between those two flows there was a large and well-defined shear layer. The corresponding vertical shear field is shown in Figure 9(c). Throughout the event there was a layer of large shear between ~ 0.8 and 2.0 km. A vertical average between these two levels was used to characterize the strength of the shear layer, which will be called the ‘mid-level shear’ (red circles in Figure 10).

Independently of the calculations presented above, we perused all the DOW radar down-valley radial velocity RHI scans obtained during the Alpine case and took notes of the times when billows like the ones shown in Figure 4(b) were observed. Although there were many instances when wavy behaviour was observed, we flagged only the instances where we were confident of the similarity to the billows in Figure 4(b). The co-evolution of the mid-level shear and the KH billows is illustrated in Figure 10. There were two major episodes of billows: between 0058 and 0229 UTC 21 October and 0626–0759 UTC 21 October. Both episodes

[§]However, for one quarter of the RHI scans, the time between collections was ~ 11 min.

[¶]The reflectivity average was conducted in logarithmic space, while the radial velocity one was conducted in linear space.

coincide with (i) large values of shear immediately before the occurrence of the billows; (ii) a decrease of the mid-level shear during the occurrence of the billows; and (iii) an intensification of the mid-level shear after the episode concluded. The apparent relationship between the trends in the mid-level shear strength and the billows episodes described here aligns well and illustrates what has been reported elsewhere in the literature. For example, Browning (1971) noted that the initiation of large-amplitude billows like the ones presented here is generally preceded by an increase in wind shear. According to Ottersten (1970), the large amplitude billows develop when small billows are no longer able to accomplish completely the rearrangement of the shear flow. Our observations also align with Houser and Bluestein (2011) who described the transfer of momentum of the KH waves and also found that they slightly reduced the local wind shear.

Although no definitive evidence of the billows was observed in the DOW's radial velocity after 0930 UTC 21 October there were suggestions of them in the spectrum width (similar to what was seen in Figure 4(d)) at times (e.g. 0958 UTC, 1356 UTC and 1513 UTC). By ~1600 UTC, the synoptic conditions were changing and the precipitation was starting to transition from stratiform to convective as the post-frontal part of the storm moved over the DOW radar site.

6. Conclusions

This study presents observational evidence of KH billows that occur within midlatitude cyclones as they move over mountain ranges, specifically the Alps and the Cascades. The KH billows, which had horizontal scales of 3–4 km, were observed in an environment that was statically stable and highly sheared. The upstream flow was characterized by $Ri < 0.25$ in layers that were slightly below the levels where the KH billows occurred. This vertical displacement suggests that the upstream flow is subjected to some orographic lifting, as was observed and suggested by Geerts and Miao (2010). During the Alpine case, the DOW radar collected detailed data inside the Toce Valley (Figure 2(b)) and it mapped a pronounced down-valley flow at levels below ~1.2 km as the flow above had a strong component toward the mountain. Between these flows, a large shear layer developed that was conducive to KH waves. The co-evolution of the shear and the billows indicates that the shear first attains large values, then the billows appear, followed by a decrease of the shear. This pattern was observed on two different episodes of KH billows. Both of the KH billows episodes lasted for about 1.5 h.

As midlatitude cyclones approach mountain ranges like the Alps, the Oregon Cascades or the Sierra Nevada, a layer of shear often occurs in air rising over the terrain when the flow is statically stable or nearly neutral. Observational studies suggest that during winter storms, a layer containing high values of vertical shear may often be a feature of high mountain ranges (e.g. Lin *et al.*, 2005; Garvert *et al.*, 2007; Neiman *et al.*, 2010; Campbell and Steenburgh, 2014). Idealized numerical simulations indicate that a shear layer develops on the windward side of a mountain as a result of strong static stability and/or surface friction. In addition, pre-existing shear (e.g. baroclinically induced) will be enhanced further over the windward slope (Medina *et al.*, 2005). The combination of statically stable or neutral flow and vertical shear foster turbulent flow and cells that concentrate upward motions, which may enhance the microphysical process of precipitation growth over the windward slopes (as proposed by Houze and Medina, 2005; Medina *et al.*, 2005; Medina and Houze, 2015). The current article indicates that the combination of vertical shear and statically stable/neutral flow may be specifically conducive to the occurrence of KH billows and suggests that they could constitute the type of turbulence observed in past studies.

Future field experiments, like the Olympic Mountains Experiment (OLYMPEX, <http://olympex.atmos.washington.edu/>), should investigate whether the occurrence of large shear, turbulent small-scale cells, and KH billows are commonly

observed when extratropical cyclones move over mountain ranges that are not two-dimensional barriers. (Preliminary results from OLYMPEX show that down-valley flow and shear occur in the Quinault Valley of the Olympic Rain Forest; but data have yet to be analysed to determine the existence of KH waves.)

Acknowledgements

This research was supported by the National Science Foundation under Grant AGS-1503155. Beth Tully processed the graphics. We would like to acknowledge two anonymous reviewers for their comments and suggestions.

References

- Aberson SD, Halverson JB. 2006. Kelvin–Helmholtz billows in the eyewall of Hurricane Erin. *Mon. Weather Rev.* **134**: 1036–1038.
- Asencio N, Stein J. 2006. Origins of the reversed flow over the windward Alpine foothills during MAP IOP3 and IOP8. *Q. J. R. Meteorol. Soc.* **132**: 297–316.
- Atlas D, Metcalf JJ, Richter JH, Gossard EE. 1970. The birth of 'CAT' and microscale turbulence. *J. Atmos. Sci.* **27**: 903–913.
- Bougeault P, Binder P, Buzzi A, Dirks R, Houze RA Jr, Kuettner J, Smith RB, Steinacker R, Volkert H. 2001. The MAP special observing period. *Bull. Am. Meteorol. Soc.* **82**: 433–462.
- Bousquet O, Smull B. 2003a. Airflow and precipitation fields within deep Alpine valleys observed by airborne Doppler radar. *J. Appl. Meteorol.* **42**: 1497–1513.
- Bousquet O, Smull B. 2003b. Observations and impacts of upstream blocking during a widespread orographic precipitation event. *Q. J. R. Meteorol. Soc.* **129**: 391–410.
- Bousquet O, Smull B. 2006. Observed mass transports accompanying upstream orographic blocking during MAP IOP8. *Q. J. R. Meteorol. Soc.* **132**: 2391–2413.
- Browning KA. 1971. Structure of the atmosphere in the vicinity of large-amplitude Kelvin–Helmholtz billows. *Q. J. R. Meteorol. Soc.* **97**: 283–299.
- Browning KA, Watkins CD. 1970. Observations of clear air turbulence by high power radar. *Nature* **227**: 260–263.
- Campbell LS, Steenburgh WJ. 2014. Finescale orographic precipitation variability and gap-filling radar potential in Little Cottonwood Canyon, Utah. *Weather and Forecasting* **29**: 912–935.
- Chapman D, Browning KA. 1997. Radar observations of wind-shear splitting within evolving atmospheric Kelvin–Helmholtz billows. *Q. J. R. Meteorol. Soc.* **123**: 1433–1439.
- Chapman D, Browning KA. 1999. Release of potential shearing instability in warm frontal zones. *Q. J. R. Meteorol. Soc.* **125**: 2265–2289.
- Dutton J, Panofsky HA. 1970. Clear air turbulence: A mystery may be unfolding. *Science* **167**: 937–944.
- Gage KS, Van Zandt TE. 1983. 'The simulation of intermittent clear air turbulence by a Monte Carlo technique'. *AMS 6th Symposium on Atmospheric Turbulence and Diffusion*, March 1983, Boston.
- Garvert MF, Colle BA, Mass CF. 2005a. The 13–14 December 2001 IMPROVE-2 event. Part I: Synoptic and mesoscale evolution and comparison with a mesoscale model simulation. *J. Atmos. Sci.* **62**: 3474–3492.
- Garvert MF, Woods CP, Colle BA, Mass CF, Hobbs PV, Stoelinga MT, Wolfe JB. 2005b. The 13–14 December 2001 IMPROVE-2 event. Part II: Comparisons of MM5 model simulations of clouds and precipitation with observations. *J. Atmos. Sci.* **62**: 3520–3534.
- Garvert MF, Smull B, Mass C. 2007. Multiscale mountain waves influencing a major orographic precipitation event. *J. Atmos. Sci.* **64**: 711–737.
- Geerts B, Miao Q. 2010. Vertically pointing airborne Doppler radar observations of Kelvin–Helmholtz billows. *Mon. Weather Rev.* **138**: 982–986.
- Houser JL, Bluestein HB. 2011. Polarimetric Doppler radar observations of Kelvin–Helmholtz waves in a winter storm. *J. Atmos. Sci.* **68**: 1676–1702.
- Houze RA Jr, Medina S. 2005. Turbulence as a mechanism for orographic precipitation enhancement. *J. Atmos. Sci.* **62**: 3599–3623.
- Kingsmill DE, Neiman PJ, Moore BJ, Hughes M, Yuter SE, Ralph FM. 2013. Kinematic and thermodynamic structures of Sierra barrier jets and overrunning atmospheric rivers during a landfalling winter storm in northern California. *Mon. Weather Rev.* **141**: 2015–2036.
- Lin Y-L, Reeves HD, Chen S-Y, Chiao S. 2005. Formation mechanism for convection over the Ligurian Sea during MAP IOP-8. *Mon. Weather Rev.* **133**: 2227–2245.
- Medina S, Houze RA Jr. 2003. Air motions and precipitation growth in Alpine storms. *Q. J. R. Meteorol. Soc.* **129**: 345–371.
- Medina S, Houze RA Jr. 2015. Small-scale precipitation elements in mid-latitude cyclones crossing the California Sierra Nevada. *Mon. Weather Rev.* **143**: 2842–2870.
- Medina S, Smull BF, Houze RA Jr, Steiner M. 2005. Cross-barrier flow during orographic precipitation events: Results from MAP and IMPROVE. *J. Atmos. Sci.* **62**: 3580–3598.

- Medina S, Sukovich E, Houze RA Jr. 2007. Vertical structures of precipitation in cyclones crossing the Oregon Cascades. *Mon. Weather Rev.* **135**: 3565–3586.
- Miles JW. 1986. Richardson's criterion for the stability of stratified shear flow. *Phys. Fluids* **29**: 3470–3471.
- Miles JW, Howard LN. 1964. Note on a heterogeneous shear flow. *J. Fluid Mech.* **20**: 331–336.
- Neiman PJ, Sukovich EM, Ralph FM, Hughes M. 2010. A seven-year wind profiler-based climatology of the windward barrier jet along California's northern Sierra Nevada. *Mon. Weather Rev.* **138**: 1206–1233.
- Neiman PJ, Hughes M, Moore BJ, Ralph FM, Sukovich EM. 2013. Sierra barrier jets, atmospheric rivers, and precipitation characteristics in northern California: A composite perspective based on a network of wind profilers. *Mon. Weather Rev.* **141**: 4211–4233.
- Ottersten H. 1970. Radar observations of the turbulent structure in shear zones in the clear atmosphere. In *Proceedings, 14th Conference on Radar Meteorology*, Tucson, AZ: 111–116. American Meteorological Society: Boston.
- Petre JM, Verlinde J. 2004. Cloud radar observations of Kelvin–Helmholtz instability in a Florida anvil. *Mon. Weather Rev.* **132**: 2520–2523.
- Reiter ER, Lester PF. 1968. Richardson's number in the free atmosphere. *Arch. Meteorol. Geophys. Bioklim. A* **17**: 1–7.
- Sha W, Kawamura T, Ueda H. 1991. A numerical study on sea/land breezes as a gravity current: Kelvin–Helmholtz billows and inland penetration of the sea-breeze front. *J. Atmos. Sci.* **48**: 1649–1665.
- Steiner M, Bousquet O, Houze RA Jr, Smull BF, Mancini M. 2003. Airflow within major Alpine river valleys under heavy rainfall. *Q. J. R. Meteorol. Soc.* **129**: 411–432.
- Stoelinga MT, Hobbs PV, Mass CF, Locatelli JD, Colle BA, Houze RA Jr, Rangno AL, Bond NA, Smull BF, Rasmussen RM, Thompson G, Colman BR. 2003. Improvement of microphysical parameterizations through observational verification experiments (IMPROVE). *Bull. Am. Meteorol. Soc.* **84**: 1807–1826.
- Turner JS. 1973. *Buoyancy Effects in Fluids*. Cambridge University Press: Cambridge, UK.
- Werne J, Fritts D. 1999. Stratified shear turbulence: Evolution and statistics. *Geophys. Res. Lett.* **26**: 439–442, doi: 10.1029/1999GL900022.
- Wurman J, Straka J, Rasmussen E, Randall M, Zahrai A. 1997. Design and deployment of a portable, pencil-beam, pulsed, 3-cm Doppler radar. *J. Atmos. Oceanic Technol.* **14**: 1502–1512.
- Zagrodnik JP, McMurdie L, Houze RA Jr. 2015. 'NPOL observations of Kelvin–Helmholtz waves during the May 2013 IFloodS campaign'. In *Proceedings of Precipitation Measuring Mission Science Team Meeting*, 13–17 July 2015, Baltimore, MD.